Sensors & Diagnostics

PAPER

View Article Online
View Journal | View Issue

Cite this: *Sens. Diagn.*, 2024, **3**, 688

Flexible & transparent breath sensor and conducting electrodes based on a highly interconnected Au nanoparticle network†

Namuni Sneha and S. Kiruthika *

In this study, transparent humidity sensors and conducting electrodes (TCEs) were fabricated using a highly interconnected gold nanoparticle network (Au nanonetwork) *via* a simple solution approach. Here, the direct reduction of metal anions at lower temperatures (5 °C) followed by the addition of a non-polar solvent facilitates the cold welding of nanoparticles at junctions and yields an interconnected Au nanonetwork at the liquid–liquid interface. The formed Au nanonetwork is cautiously transferred to the desired flexible, stretchable, and transparent substrates for various applications. As the synthesis involves no capping agents, the prepared nanonetworks offer high conductivity without further chemical or thermal treatments. The fabricated Au nanonetwork is highly crystalline and thermally stable, with excellent mechanical robustness towards various deformations. Using an Au-1L (1-layer) nanonetwork, a highly transparent (>85%) humidity sensor is fabricated with short response and recovery times (1.1 s and 1.3 s). The Au-1L sensor is studied systematically for various humidity changes (40% to 90%) and breath conditions (normal/deep, hydrated/dehydrated, breathing/blowing, *etc.*) and exhibits high selectivity toward humidity. Notably, the sensing device offered a stable response for more than a year demonstrating its robustness for prolonged use.

Received 14th December 2023,
Accepted 15th February 2024

DOI: 10.1039/d3sd00330b

rsc.li/sensors

Introduction

Transparent electronics has emerged as a highly promising and innovative field focused on developing electronic devices and even their components with high transparency, flexibility, and stretchability.[1,2] Recently, transparent soft robots have attracted huge interest and found enormous use in healthcare and human–machine interactions.[3–5] Transparent energy storage devices are crucial for integrating into (transparent) energy-harvesting devices,[2,6–8] whereas transparent heaters are used to selectively heat transparent surfaces without obstructing visibility.[9–11] Transparent air filters are specifically designed for applications where maintaining transparency is quite essential.[12,13] In this scenario, transparent sensors are crucial for applications where seamless integration is required upon transparent surfaces.[14–16]

Current technology immensely demands wearable breath sensors with high sensitivity and selectivity besides being visibly transparent and with excellent mechanical flexibility as they have the potential to monitor our routine healthcare with great aesthetic appeal.[17] Transparent and robust breath sensors signify a vital connection between nanotechnology and healthcare, and they are demanded in scenarios where see-through devices are required.[18] Diverse materials have been extensively studied to develop robust breath-sensing devices with ultra-sensitivity, long-term stability, and rapid response and recovery capabilities. These innovative devices can detect and monitor various environmental humidity conditions and abnormalities in human exhaled breath. A healthy adult breathes 12–20 times per minute.[19–21] The changes in the breath rate can be associated with a few medical conditions like breathing pattern disorders, chronic obstructive pulmonary disease,[22] sleep apnea,[23] *etc.*[24,25] Early detection helps clinicians provide timely treatments and reduces the risk of health complications.[26] Breath sensors sensitive to volatile organic compounds (VOCs) can help in detecting metabolic disorders and certain cancers by analyzing the breath at an early stage.[27,28] After the COVID-19 pandemic, there has been a huge surge in the development of breath sensors for rapid and non-invasive detection of the virus.[29]

Susceptible humidity/breath sensors with rapid response and recovery were generally fabricated using functional materials like carbon nanotubes (CNTs),[30,31] metal oxides (SnO_2, ITO, V_2O_5),[32–37] metal oxysulfide ($WS_2|O$),[38] graphene,[26,39] conducting polymers,[40,41] *etc.* The devices were fabricated by coating these materials over the desired substrates using various techniques such as vapor deposition

Department of Physics, School of Electrical and Electronics Engineering, SASTRA Deemed to be University, Thanjavur 613 401, Tamil Nadu, India.
E-mail: kiruthika@ece.sastra.edu

† Electronic supplementary information (ESI) available: XPS core level spectra of C1s and O1s, XRD pattern of as-prepared Au-5L, transmittance and *I–V* characteristics of the Au nanonetwork, and breath response of the Au-1L sensor. See DOI: https://doi.org/10.1039/d3sd00330b

(physical and chemical),[31,42,43] printing (inkjet, screen, hydrothermal),[26,44–46] lithography approaches,[47,48] *etc.* Usually, producing high-quality CNTs on a large scale is quite expensive and challenging as it requires catalysts and high-temperature processing conditions.[49] Although metal oxides are easy to synthesize and often cost-effective, they are brittle and prone to fracture under stress, further limiting their use in flexible devices.[50] Although metal oxysulfides offer more robustness towards flexibility, they suffer from complex synthesis methods to have control over stoichiometries (of oxides and sulfides) and their purity.[38,51] Graphene, a 2D material, is extensively used in breath sensing due to its high sensitivity. However, it offers limited selectivity and slow recovery times which affect the sensor's accuracy and reliability.[52] On the other hand, conducting polymers offer slower responses limiting their use in rapid detection requirements. Furthermore, conducting polymers have only limited effective working temperature ranges.[50] The sensors fabricated using metal wire networks provide a robust and technologically viable solution for diverse applications in wearable electronics. They offer several advantages, including enhanced durability, reliability, and flexibility, enabling the devices to adapt to the body's natural movements.

Metal nanonetworks can be synthesized through solution-based methods, like the sol–gel process[53] and electroless deposition.[54] The sol–gel method often involves multiple steps and prolonged reaction duration.[55] Electroless deposition offers benefits like cost-effectivity, conformal coating, and scalability, but it requires templates for controlling the network architecture.[56] It also suffers from issues related to agglomeration and control over particle size.[56] The liquid–liquid interface technique emerged as a versatile approach for synthesizing various metal particle networks. This method involves mixing two immiscible liquid phases, typically aqueous and organic, wherein metal precursors undergo controlled reduction, forming nanoparticle networks at the interface. Besides supporting large-scale production, of course, limited by bath sizes, it also provides precise control over nanoparticle size and surface functionalization. This method is often used for synthesizing thin films[57,58] as well as networks of metal[59,60] and metal oxide nanoparticles[61] which are further transferred to the desired substrates for various optoelectronic applications. Although metal networks offer several advantages like high electrical conductivity and flexibility, semi-noble metals such as copper and silver are highly prone to oxidation when exposed to moisture leading to a decrement in electrical conductivity and degradation of performance. In this regard, gold nanoparticle networks overcome all such shortcomings and deliver a significant advantage in modern electronic devices.

In this work, a highly interconnected Au nanonetwork is fabricated through a complete solution approach at the liquid–liquid (organic and aqueous) interface. As the synthesis process is quite simple and involves no high-temperature annealing, the formed nanonetwork can be easily transferred to flexible and transparent substrates, including PET, PDMS, and paper. Thus, the prepared Au nanonetworks were further studied for breath sensing and transparent conducting electrode (TCE) applications. By controlling the loading of Au network layers, the transmittance and sheet resistance of the prepared electrodes can be precisely varied. The existence of nanogaps across the single-layer gold nanoparticle network (Au-1L) was further utilized for the fabrication of transparent humidity and breath-sensing devices. The liquid–liquid interface method offers a promising and convenient approach for synthesizing Au nanonetworks, enabling potential applications in various fields of transparent electronics and sensing devices.

Experimental

Materials

Gold chloride trihydrate ($HAuCl_4 \cdot 3H_2O$, ultrapure 99.99%), sodium borohydride ($NaBH_4$, extra pure 98%), toluene ($C_6H_5CH_3$, 99%), ethanol (C_2H_5OH, 99.9%), isopropyl alcohol (C_3H_8O, pure 99%), acetone (C_2H_6CO, extra pure 99%), and *n*-hexane (C_6H_{14}, pure 99%) were purchased from SRL Chemicals, India. Sulfuric acid (H_2SO_4, lab reagent) and hydrogen peroxide (H_2O_2, 30%) were obtained from Isochem Pvt. Ltd. The glass slides used in the experiments were purchased from Blue Star Pvt. Ltd, India. PET (polyethylene terephthalate) sheets with a thickness of 100 microns were obtained from Asian Reprographics (P) Ltd., India. For preparing the polydimethylsiloxane (PDMS) substrates, the Sylgard 184 curing agent and elastomers were procured from Dow Corning. All chemicals and materials were used without further purification.

Characterization

The size of the Au nanoparticles was analyzed using a transmission electron microscope (TEM) from FEI Tecnai f20. A scanning electron microscope (SEM) from TESCAN Vega 3, Czech Republic was employed to study the morphology of Au nanonetworks. For elemental and chemical state analysis, an X-ray photoelectron spectrometer (XPS) from Thermo Scientific, UK (K-ALPHA source) was utilized. X-ray diffraction (XRD) was carried out using a Bruker D8 Focus instrument to investigate the crystallinity of the prepared Au nanonetworks. To measure the transmittance properties of the electrodes, a PerkinElmer UV–visible spectrophotometer was used. The electrical sheet resistances of the electrodes were evaluated using a homemade four-point probe setup (with a probe width of 0.5 mm and a distance of 2 mm between the copper probes) and a GWINSTEK-GDM-360 TRMS digital handheld multimeter. To investigate the humidity sensing properties of the device, a custom-designed setup has been arranged. The *I–V* characteristic and breath sensing analyses were conducted using an electrochemical workstation, the CorrTest Model CS150. For breath analysis, the device was connected to the electrochemical workstation. The reference and counter electrodes were connected to one end, whereas the working electrode was connected to the other end of

the device. All experiments were performed in accordance with the guidelines approved by the ethics committee at SASTRA Deemed University. Informed consent was obtained from human participants of this study. To test the sensor's selectivity, volatile gases were directly purged over the device, and the response was recorded. An iSTIR HP550 PRIME hotplate was used to evaluate the electrodes' thermal stability. Optical microscopy images were captured using a NIKON ECLIPSE LV100ND.

Substrate treatments

The glass substrates were cleaned in a piranha solution composed of sulfuric acid (H_2SO_4) and 30% hydrogen peroxide (H_2O_2) in a 3 : 1 ratio for an hour, followed by washing in DI water to remove contaminants completely. PET sheets were thoroughly cleaned with soap solution, DI water, isopropyl alcohol, and acetone, respectively. PDMS substrates were prepared by mixing the Sylgard 184 curing agent and elastomer in a ratio of 1 : 10. This mixture was thoroughly degassed to remove any trapped air bubbles and then poured over a smooth surface and left to cure at room temperature for 24 hours. After curing, the desired dimensions were cut and thoroughly cleaned with hexane, followed by ethanol.

Preparation of the Au nanonetwork at the liquid–liquid interface

Au nanonetworks were synthesized at the liquid–liquid interface using a complete solution approach, as shown in Fig. 1. First, an aqueous gold chloride solution (aq. $HAuCl_4$) was prepared by dissolving 1 mM auric chloride ($HAuCl_4 \cdot 3H_2O$) in 25 mL of DI water. Later, the prepared aqueous $HAuCl_4$ solution was then subjected to cooling at 5 °C. To reduce the gold chloride, a strong reducing agent sodium borohydride ($NaBH_4$, 7.4 mM, 25 mL) was added dropwise at a stirring speed of 600 rpm over 1 hour. The addition of the reducing agent initiates the gold nanoparticle formation which is evident from its color change from yellow to wine-red. Subsequently, the formed gold nanoparticle solution was mixed with 100 mL of toluene at 5 °C and vigorously stirred for 10 min. This process enabled the transfer of the gold nanoparticles from the aqueous phase to the liquid–liquid interface, where they underwent cold welding together to form a well-defined gold nanonetwork.[59]

Following this, the setup was brought to room temperature. After 30 minutes, the toluene layer was carefully removed without disturbing the welded nanonetwork, leaving a thin residual layer (~2 mL in the crystallizing dish with a size of 100 × 50 mm) above the aqueous surface. For further studies, the highly interconnected nanonetworks were transferred onto substrates such as piranha-treated glass, cleaned PET, or PDMS and were annealed at 100 °C for 15 minutes to enhance their adhesion and stability.

Results and discussion

Highly interconnected conducting Au nanonetworks were obtained at the liquid–liquid interface *via* a complete solution approach (Fig. 1). The synthesis procedure begins

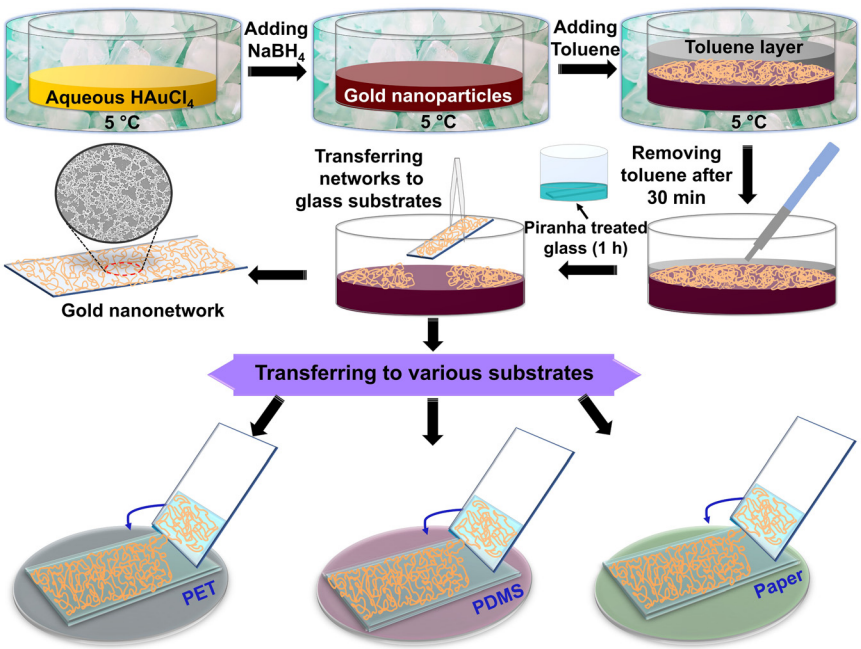

Fig. 1 Schematic illustrating the synthesis of the gold nanoparticle network (Au nanonetwork for brevity) at the liquid–liquid interface *via* direct reduction of metal ions with a strong reducing agent with no capping agent. The Au nanonetworks were obtained by reducing gold chloride with sodium borohydride at 5 °C, subsequently followed by the addition of a non-polar toluene solvent. The formed Au nanonetworks at the liquid–liquid interface can be potentially transferred to any desired pre-treated substrates after removing the toluene layer.

by reducing the cold auric chloride solution (5 °C) with sodium borohydride, a strong reducing agent, to form gold nanoparticles which were further evidenced by the change in the color of the reaction medium to wine-red. To the above nanoparticle solution, toluene, a non-polar solvent, was added while maintaining it at 5 °C and continued vigorous stirring for 10 min. Here, the toluene can effectively act as a natural stabilizing agent and avoid the necessity for supplementary capping agents.[59] The solution was then left undisturbed for 30 minutes at room temperature to allow the gold nanoparticles to slowly assemble at the liquid–liquid (aqueous–organic) interface and cold-weld. By carefully adopting these procedures, a highly robust nanonetwork was prepared at the interface. After 30 minutes, the toluene layer was carefully removed without disturbing the formed nanonetwork at the interface. Letting the toluene layer for complete evaporation under ambient conditions led to the shattered Au network with breakage in the connections.

The successful transfer of the Au nanonetwork from the interface onto flexible, stretchable, and transparent substrates plays a vital role as it decides the diverse use of Au nanonetworks in wearable electronics. However, transferring to the desired substrates is associated with specific challenges like slippage, poor adhesion to the glass substrate, non-uniform coating, *etc.* In order to overcome these issues, piranha-treated glass substrates were preferred. Lifting off with piranha-treated glass offers better spreading and adhesion of the Au nanonetwork towards the substrate as the piranha treatment immensely cleanses the substrate surface, making it more hydrophilic besides improving the adhesion onto the glass substrates. After every lift-off process, the Au-nanonetwork/glass was annealed at 100 °C for 15 min to improve its adhesion before passing again into the liquid–liquid interface. Here, the layers were numbered after the number of networks stacked. Although piranha treatment is effective for glass substrates, issues related to transferring the network onto substrates like PET, PDMS, paper, *etc.* still remain. To address this limitation, the network from the interface was first lifted onto a piranha-treated glass substrate with a minimal amount of aqueous layer and carefully transferred to the desired substrates (PET/PDMS/paper). The transfer process involves careful sliding of the network to the desired substrate, ensuring the seamless integration of the network (Fig. 1). By employing this strategy, the challenges associated with the specific transfer of interconnected networks onto different substrates were overcome, ensuring optimal adhesion for further studies. The transfer protocol also supports achieving multi-layer coatings by stacking (up to Au-12L) to achieve lower sheet resistances through improved interconnectivity.

The bright-field transmission electron microscopy (TEM) images of the Au-1L (1 layer) nanonetwork, formed at the liquid–liquid interface, were collected over a carbon-coated copper grid. The TEM grid was gently immersed into the liquid–liquid interface to collect the Au nanonetwork. Subsequently, the grid was carefully dried on a hot plate for 15 min at 100 °C. The TEM analysis and selected area electron diffraction (SAED) pattern confirmed the crystallinity and interconnectivity of the Au nanonetworks (Fig. 2a–c). From scanning electron microscopic images (Fig. 2d), it is understood that the interconnected Au-1L nanonetwork is dispersed uniformly with a low fill factor which is attributed to its higher transmittance. In addition, the Au-1L nanonetwork is non-conducting, which might be due to the presence of nanogaps between the Au particles. This network is further used in breath and humidity sensing which will be discussed later. Fig. 2e and f present the SEM images of highly interconnected dense Au-12L nanonetworks at different magnifications. To understand the chemical composition of the Au-1L nanonetwork

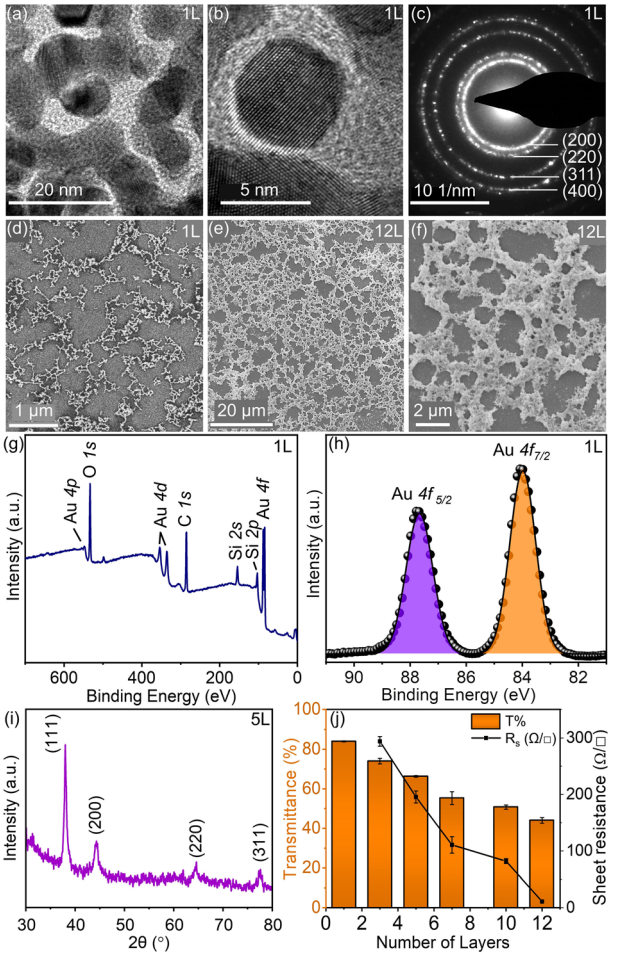

Fig. 2 (a and b) Low and high-resolution transmission electron microscopy images, and (c) selected area electron diffraction (SAED) pattern of the Au-1L nanonetwork collected over the carbon-coated copper grid. (d–f) Scanning electron microscopy images of Au-1L and Au-12L nanonetworks at different magnifications. (g) X-ray photoelectron survey spectrum of the Au-1L nanonetwork. (h) XPS core level spectrum of Au 4f. (i) XRD pattern of the Au-5L network after rinsing with DI water. The peak positions match well with JCPDS file no. 04-0784. (j) Comparison of the transmittance (%) (at 550 nm) and sheet resistances (in $\Omega\ \square^{-1}$) of the synthesized electrodes with various stacked layers of the Au nanonetwork.

collected on a glass surface, XPS analyses were performed. Fig. 2g shows a high-resolution survey spectrum of the Au-1L nanonetwork coated over a glass substrate. The spectrum indicates major elemental peaks for Au (Au 4f, Au 4d & Au 4p), carbon (C 1s), silicon (Si 2s, Si 2p), and oxygen (O 1s). The silicon and oxygen peaks appeared due to the glass substrate. The high-resolution core level spectrum of Au 4f (Fig. 2h) exhibited a doublet with binding energies of 83.9 eV and 87.6 eV, corresponding to Au $4f_{7/2}$ and Au $4f_{5/2}$, respectively.[62] The elemental peaks for C 1s and O 1s are shown in Fig. S1.† In addition, X-ray diffraction analyses were performed further to confirm the crystalline nature of the nanonetwork (Au-5L). The XRD pattern of the as-prepared Au-5L network indicated the presence of NaCl along with Au (Fig. S2†), which was later removed by gentle rinsing with water (Fig. 2i). By varying the number of stacking layers of the Au nanonetwork (1L to 12L) from the liquid–liquid interface, the transmittance and sheet resistance of the resulting TCEs are finely tuned (Fig. 2j). The transmittance (T%) spectra, I–V characteristics and photographs of the various Au stacked layers are shown in Fig. S3 and S4.†

The thermal stability of the prepared transparent conducting electrodes was analyzed by annealing them at high temperatures (up to 300 °C). The variation in sheet resistances of various lift-off layers (Au-3L to Au-12L) with respect to annealing temperatures is shown in Fig. 3a. In general Au-5L and beyond, the electrodes exhibit more stability towards high-temperature treatments. However, for Au-3L, the sheet resistance decreases with the increase in temperature which might be due to the decrement in the junction resistance.[9,10] Stretchable and flexible electrodes have significant demand in wearable electronics, and they should offer more robustness in maintaining their electrical conductivity under various mechanical stimuli. To study the suitability of the prepared Au-TCE for flexible electronic applications, Au-12L (Rs = 11.2 Ω $\square^{-1}$) was prepared over PDMS substrates and it was stretched to different strains (0% to 100%) in two different directions (parallel and perpendicular to the Ag contacts) as demonstrated in the inset of Fig. 3b. The TCE has shown outstanding stability towards the entire strain range from 0 to 100% in both directions evidencing the strong binding of the Au nanonetwork towards PDMS substrates. In addition, it also proves its insensitivity in electrical resistance towards various mechanical deformations. The optical microscopy image of Au-12L over the PDMS substrate is shown in Fig. S5.† The mechanical stability of the prepared Au nanonetwork (Au-12L/PET) was tested by repeatedly bending it to various bending radii (2, 3.5, and 5 mm). Even after 1000 bending cycles with a 2 mm bending radius, only less than 6% increment in resistance was noticed, whereas for 3.5 and 5 mm bending radii, 2.7% and 0.7% increments were observed, respectively (Fig. 3c). Although the TCEs have shown excellent mechanical robustness towards stretching and bending tests, the Au nanonetwork's adhesion to glass substrates showed substandard results during the scotch tape adhesion test (see Fig. S6†). However, this limitation could be overcome by coating any protective layer over the TCE.

To fabricate a transparent breath-sensing device, Au-1L was chosen as it offers a drastic change in resistance when exposed to humidity due to the existence of nanogaps between Au nanonetworks. Fig. 4a presents the optical transmittance spectrum of the Au-1L nanonetwork (glass substrate), exhibiting a high transmittance of about 86.6% at 550 nm and an average transmittance of 87% between 400 and 1000 nm. The inset in Fig. 4a is a photograph of the

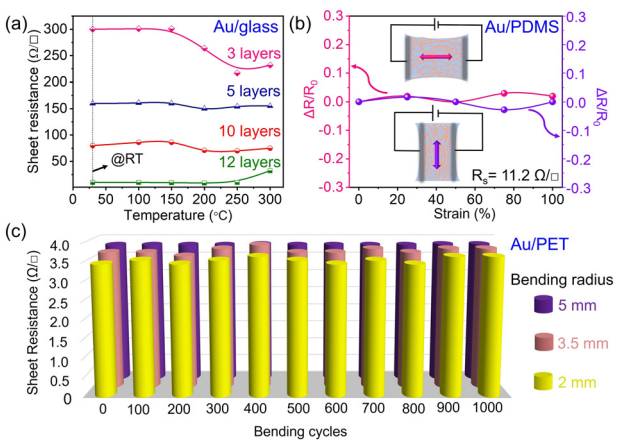

Fig. 3 Thermal and mechanical durability of Au nanonetwork-based TCEs. (a) The variation in sheet resistance of different Au nanonetwork electrodes when annealed to higher temperatures (till 300 °C). (b) Relative change in resistance of Au/PDMS electrodes while applying various strain% in different directions. (c) The change in sheet resistances of Au/PET electrodes while bending to different radii (2, 3.5, and 5 mm) for 1000 cycles.

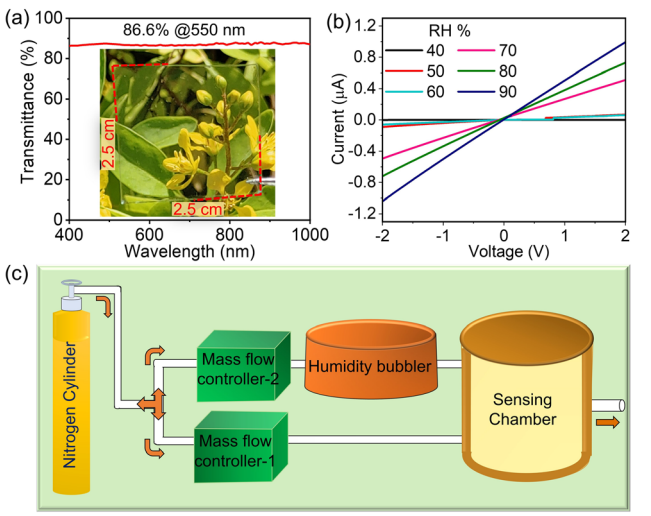

Fig. 4 (a) Transmittance spectrum of the Au-1L nanonetwork-based breath sensor from 400 to 1000 nm. Inset is the photograph of the transparent breath-sensing device (2.5 × 2.5 cm^2). (b) I–V characteristics of the transparent breath sensor (Au-1L) when exposed to different relative humidities (40–90%). (c) Schematic illustrating the testing system used for the humidity sensing measurements.

highly transparent Au-1L nanonetwork. The transmittance was measured across the device's different locations to study the Au nanonetwork's uniformity over the substrate. The resulting transmittance values (%) at 550 nm are depicted as the contour plot in Fig. S7.† From the contour plot, it is inferred that the Au-1L nanonetwork exhibits a consistent transmittance of >80% across different regions. The grid pattern drawn over the photo of Au-1L in Fig. S7† indicates the specific pixel region utilized for transmittance measurements. The transmittance spectra of five Au-1L nanonetworks (Fig. S8a†), prepared in different batches under similar experimental conditions, and their transmittance at 550 nm are compared in Fig. S8b.† As depicted in the histogram (Fig. S8b†), the variation in T% is relatively less. The standard deviations of T% (at 550 nm) for all five devices are 84.34 ± 1.35%. While exposing the Au-1L device to various relative humidities, a drastic increase in the current based on RH% was observed. Fig. 4b presents the I–V characteristics of the device (Au-1L) when exposed to varying relative humidity (RH%) from 40% to 90%. The custom-designed setup used for humidity sensing is shown in Fig. 4c. The required humidity environment was created inside the chamber by adjusting the flow rate of mass flow controller-1. The sensor (Au-1L) was then exposed to nitrogen gas using mass flow controller-2 at a flow rate of 2000 sccm to obtain a suitable baseline of the sensor, *i.e.*, below <5%.

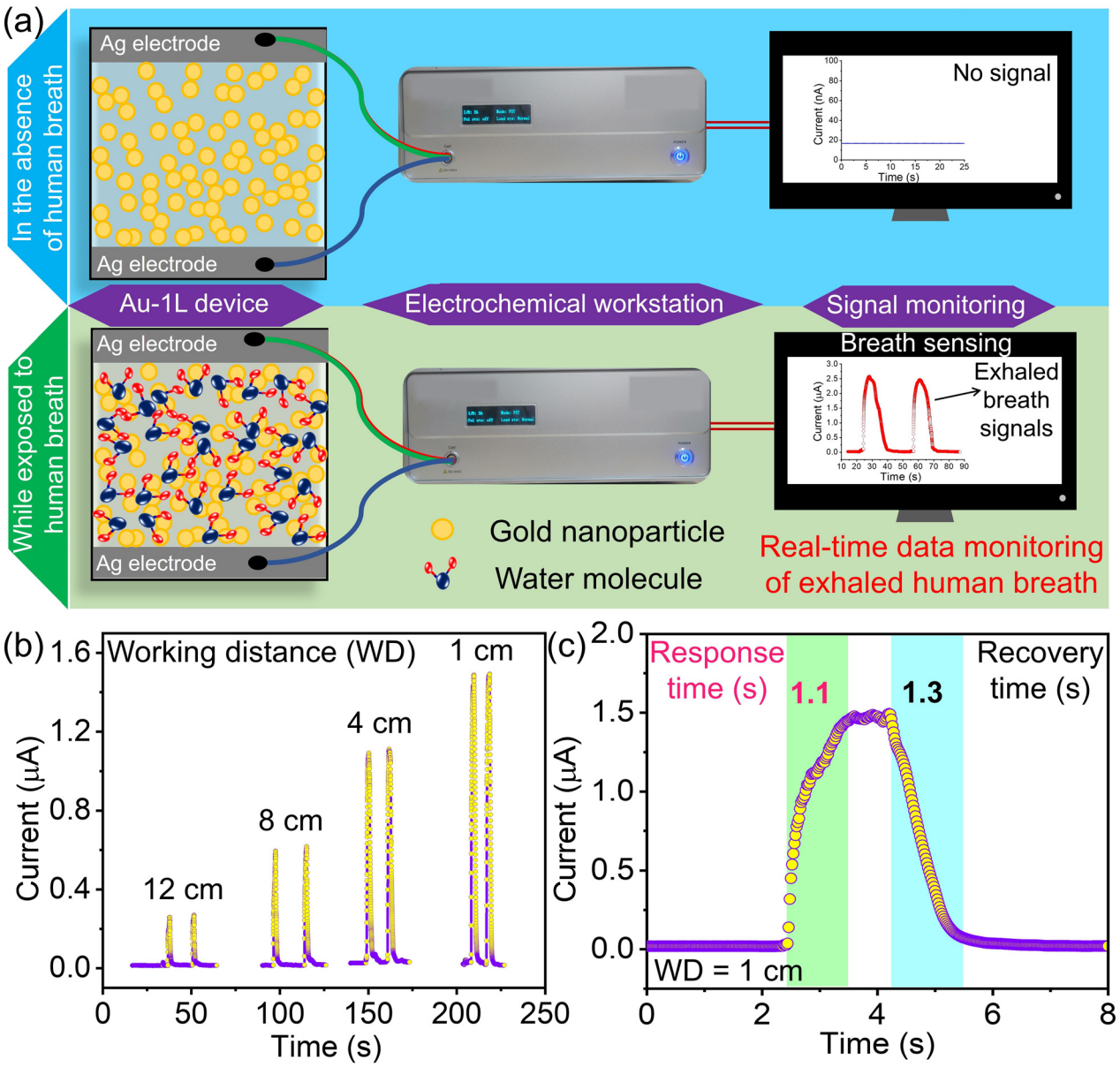

Fig. 5 (a) Schematic illustrating the working mechanism of the Au-1L nanonetwork-based breath sensor using an electrochemical workstation. The device shows a significant response when exposed to humidity in the human breath. (b) The plot shows the change in the current of the breath sensor while operating at different working distances (WDs) ranging from 1 to 12 cm. (c) The breath response curve depicts the quick response and recovery nature of the Au-1L breath sensor.

Later, the flow rate of mass flow controller-2 was set to zero to obtain the response towards the humidity. Further, by varying humidity (RH%) the sensor response was studied. *I–V* characteristics of the Au-1L device before and while exposed to 90% RH is shown in Fig. S9.† The humidity sensing behavior of the device in the presence of various relative humidities (RH%) is shown in Fig. S10.†

Fig. 5a illustrates the mechanism of breath sensing and real-time data monitoring of the Au-1L sensor using a simple electrochemical workstation. In the absence of human breath, the Au-1L sensor has a high resistance of several hundred mega ohms, possibly due to nanogaps across the Au nanonetworks. When exposed to human breath, the humidity around the device is rapidly altered, resulting in the change in the current of the sensor (Fig. 5a). Actually, the moisture in the human breath fills the nanogaps across the Au-1L network and subsequently raises the current flow in the sensor. In Fig. 5b, the dependence of the response current towards the working distance (distance between the sensor and nose) is studied in detail. It is observed that the response current was high for shorter working distances (1 cm), which might be due to more moisture being focused and exposed over the sensor device. In contrast, the recorded response current is low for higher working distances (12 cm). Fig. 5c is a human breath signal of an Au-1L-based humidity sensor with a 1 cm working distance. The sensor exhibits rapid response to human breath and reaches a plateau of the high current zone (R ~3 MΩ) within a second and reverts to its original high resistance within 1.3 seconds. The standard deviation values of the response and recovery times of consequently monitored 20 cycles of breath signals are 1.1 ± 0.31 s and 1.3 ± 0.43 s, respectively. It is observed that the sensor data are highly reproducible and reliable.

Besides the heart rate, blood pressure, and temperature of the body, the respiratory rate is one of the four vital signs of the human condition.[63] An abnormal respiratory rate is often linked to oxygen levels in the human body, and it may signify insufficient oxygen transfer during breathing.[64] This condition may also signify various medical conditions such as respiratory infections, lung diseases, or cardiac problems.[65,66] Regular monitoring of the patient's breathing pattern provides valuable information to healthcare professionals to identify potential issues before they become critical. Au-1L-based sensors can be potential diagnostic tools to identify the various breathing trends in the patient's respiratory patterns. A series of tests were performed in order to gain a comprehensive understanding of diverse breathing patterns. Fig. 6a displays the detected responses of the sensor for different breathing rates such as normal and deep breathing. It is identified that deep breathing exhibits a higher response current, as a consequence of the sensor being exposed to a higher amount of moisture (Fig. 6a). It is also noticed that the sensor offered a higher response for hydrated situations of individuals compared to dehydrated situations. Thus, this sensor might help to examine the patient's hydrated level while monitoring continuously (see Fig. 6b). Furthermore, the device also differentiates between breathing out through the nose and the mouth (Fig. S11†). The current variation of the sensor during exhalation through the mouth is slightly higher than that through the nose, revealing that more water molecules are captured by the device while breathing out through the mouth. The graph in Fig. 6c depicts the breath response of various volunteers in the age group of 20–30 years in both gender groups. A sensor should possess high stability and offer consistent readings over time for real-life applications. Using the fabricated sensor, continuous 100 human breath exhalations were recorded, and it was noticed that there was no significant change in the response current as well as in the response and recovery times (Fig. 6d and e).

The transferred Au-1L nanonetwork onto various flexible and stretchable substrates like PET, PDMS, and paper can enhance the integration of sensors in numerous wearable and flexible electronics. One can choose the substrate that best suits the particular requirement of the wearable sensor. The photographs of the Au-1L nanonetwork on PET, PDMS, and paper are shown in Fig. 6f, and their respective respiratory signals are shown in Fig. 6g. To test the mechanical robustness of the fabricated Au-1L (PET) sensor, it was subjected to continuous bending at a 3 mm bending radius. After every 20 bending cycles, the breath response was recorded and is shown in Fig. 6h. It is noticed that the device was stable and offered constant response current throughout the experiment (see Fig. 6h). To understand more about the long-term stability of the Au-1L sensor, the device was stored under ambient conditions, and its performance was analyzed periodically. It is clearly evident that there is no change in the response current even after 1 year (see Fig. 6i). To test the thermal stability of the device at higher temperatures, the breath sensor was subjected to annealing at 500 °C for 30 minutes. After cooling down to room temperature, the breath response of the device was recorded. It is clear that there is a slight decrement in the response current with the increase in the response and recovery times by 1 s and 1.5 s, respectively (Fig. 6j).

The response of the Au-1L-based breath sensor is calculated using the following equation (eqn (1)).[67]

$$\text{Response} = (I/I_0) \quad (1)$$

where I is the current after exposure to breath and I_0 is the initial current of the sensor.

The response of the Au-1L breath sensor for normal breathing conditions (refer to Fig. 5c) is calculated to be 107. It is noteworthy to mention that our humidity/human breath sensing device exhibits fast response and recovery times with higher transmittance compared to other transparent humidity/breath sensors (Table S1†). The selectivity of humidity sensors in the presence of various volatile organic gases is an important factor in their performance, especially in applications where accurate humidity measurements are essential. The selectivity of the fabricated sensor towards human exhaled breath and other organic vapors such as acetone, chloroform, methanol,

ethanol, formaldehyde, hexane, and toluene, as well as ammonia, is discussed in Fig. 6k. It is observed that the sensor shows negligible response towards other chemical vapors compared to humidity (Fig. 6l and m).

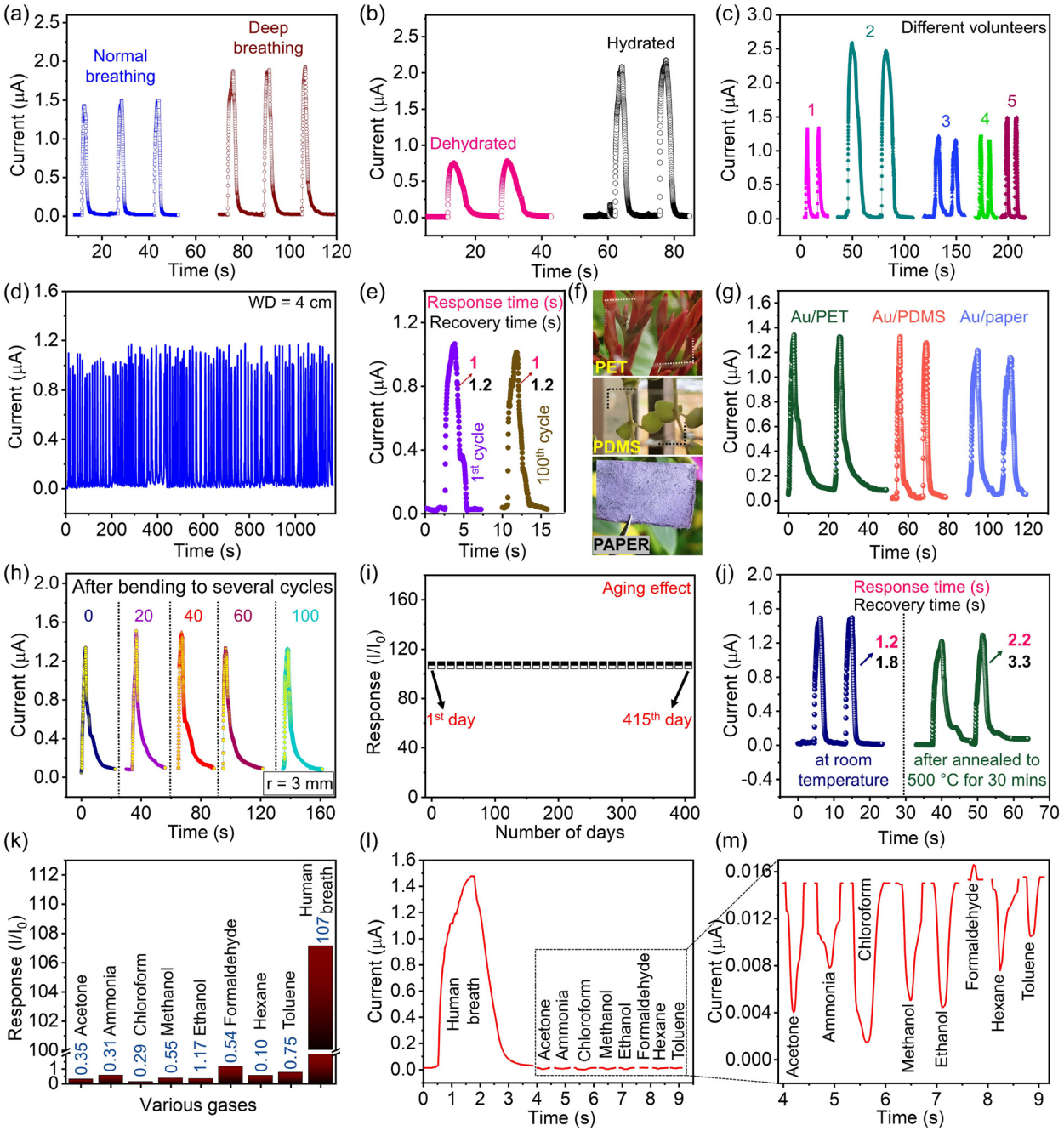

Fig. 6 Robustness of the Au-1L-based breath sensing device. (a) The plot shows the breath response pattern of an adult while breathing normally and deeply. (b) The change in breathing responses when a person is dehydrated for 3 h and hydrated. The measurements were taken after 5 minutes of consuming water. (c) Comparison of the breath-sensing response of 5 different adult volunteers. (d) Plot showing the cyclic stability of the breath sensor while continuously monitoring the breath of an individual at a working distance of 4 cm. (e) Comparison of the signals of the 1st and 100th breathing cycles demonstrating the stable output of the breath sensor. (f) Photographs of the Au-1L nanonetwork transferred to various flexible substrates like PET, PDMS, and paper. (g) The response curves of Au/PET, Au/PDMS, and Au/paper nanonetwork devices at a working distance of 1 cm. (h) The response curves of the Au-1L/PET device while bending to a 3 mm bending radius for 100 cycles. After every 20 bending cycles, the breath response was recorded and compared. (i) The plot shows the consistent response of the breath sensor while stored under ambient conditions and tested for more than a year. (j) Studying the thermal stability of the sensing device from room temperature to 500 °C. In (e) and (j), the numbers in pink and black correspond to the response and recovery times, respectively. (k) The histogram illustrating the selectivity of the sensor device towards human breath compared to other volatile organic solvents (working distance = 1 cm). (l) and (m) The variation in the current of the breath sensor when exposed to various chemical vapors and human breath (working distance = 1 cm).

Conclusions

In summary, flexible transparent humidity/breath sensors and conducting electrodes were successfully fabricated using a liquid–liquid interface approach. The Au nanonetwork obtained by this versatile approach is highly interconnected, crystalline, and easy to transfer onto the desired substrates besides being highly transparent and conducting with excellent stability towards deformations. The transmittance and sheet resistance of the TCEs are finely adjusted with the number of stacking layers (Au-3L to Au-12L). A transparent breath sensor (~86%) based on the Au-1L nanonetwork demonstrates exceptional selectivity to humidity and stability over long-term use (>1 year). The synthesis conditions also highly support the device fabrication over a wide range of substrates like glass, PET, PDMS, paper, *etc.* Moreover, the Au-1L transparent breath sensor offers short response and recovery times (1.1 s and 1.3 s) and thus may be ideal for real-time monitoring applications in smart wearable electronics.

Author contributions

S. Kiruthika: conceptualization, formal analysis, funding acquisition, writing – review & editing. Namuni Sneha: formal analysis, data curation, writing – original draft.

Conflicts of interest

There are no conflicts to declare.

Acknowledgements

The authors thank Prof. Giridhar U. Kulkarni, President, JNCASR, Bangalore, for his constant encouragement. S. K. acknowledges the funding from the SERB POWER Grant (SPG/2020/000442) and N. S. acknowledges the SERB POWER Grant for her fellowship. The authors thank Prof. Ritu Gupta, IIT Delhi, for her help in humidity measurements. The authors acknowledge SASTRA Deemed University for its support and encouragement.

References

1 J. H. Park, S. Han, D. Kim, B. K. You, D. J. Joe, S. Hong, J. Seo, J. Kwon, C. K. Jeong, H. Park, T. Kim, S. H. Ko and K. J. Lee, *Adv. Funct. Mater.*, 2017, **27**, 1701138.
2 S. Kiruthika, N. Sneha and R. Gupta, *J. Mater. Chem. A*, 2023, **11**, 4907–4936.
3 H. Lee, H. Kim, I. Ha, J. Jung, P. Won, H. Cho, J. Yeo, S. Hong, S. Han, J. Kwon, K.-J. Cho and S. H. Ko, *Soft Robot.*, 2019, **6**, 760–767.
4 P. Won, K. K. Kim, H. Kim, J. J. Park, I. Ha, J. Shin, J. Jung, H. Cho, J. Kwon, H. Lee and S. H. Ko, *Adv. Mater.*, 2021, **33**, 2002397.
5 H. Kim, H. Lee, I. Ha, J. Jung, P. Won, H. Cho, J. Yeo, S. Hong, S. Han, J. Kwon, K. Cho and S. H. Ko, *Adv. Funct. Mater.*, 2018, **28**, 1801847.
6 H. Lee, S. Hong, J. Lee, Y. D. Suh, J. Kwon, H. Moon, H. Kim, J. Yeo and S. H. Ko, *ACS Appl. Mater. Interfaces*, 2016, **8**, 15449–15458.
7 H. Moon, H. Lee, J. Kwon, Y. D. Suh, D. K. Kim, I. Ha, J. Yeo, S. Hong and S. H. Ko, *Sci. Rep.*, 2017, **7**, 41981.
8 S. Kiruthika, C. Sow and G. U. Kulkarni, *Small*, 2017, **13**, 1701906.
9 S. Kiruthika, R. Gupta and G. U. Kulkarni, *RSC Adv.*, 2014, **4**, 49745–49751.
10 R. Gupta, K. D. M. Rao, S. Kiruthika and G. U. Kulkarni, *ACS Appl. Mater. Interfaces*, 2016, **8**, 12559–12575.
11 S. Hong, H. Lee, J. Lee, J. Kwon, S. Han, Y. D. Suh, H. Cho, J. Shin, J. Yeo and S. H. Ko, *Adv. Mater.*, 2015, **27**, 4744–4751.
12 S. Han, J. Kim, Y. Lee, J. Bang, C. G. Kim, J. Choi, J. Min, I. Ha, Y. Yoon, C.-H. Yun, M. Cruz, B. J. Wiley and S. H. Ko, *Nano Lett.*, 2022, **22**, 524–532.
13 S. Jeong, H. Cho, S. Han, P. Won, H. Lee, S. Hong, J. Yeo, J. Kwon and S. H. Ko, *Nano Lett.*, 2017, **17**, 4339–4346.
14 P. Won, J. J. Park, T. Lee, I. Ha, S. Han, M. Choi, J. Lee, S. Hong, K.-J. Cho and S. H. Ko, *Nano Lett.*, 2019, **19**, 6087–6096.
15 D. Won, J. Bang, S. H. Choi, K. R. Pyun, S. Jeong, Y. Lee and S. H. Ko, *Chem. Rev.*, 2023, **123**, 9982–10078.
16 S. Kiruthika, S. Singh and G. U. Kulkarni, *RSC Adv.*, 2016, **6**, 44668–44672.
17 T. Hussain, S. Ullah, R. Fernández-García and I. Gil, *Sensors*, 2023, **23**, 7518.
18 H. Ma, H. Fang, W. Wu, C. Zheng, L. Wu and H. Wang, *RSC Adv.*, 2020, **10**, 25467–25474.
19 T. Flenady, T. Dwyer and J. Applegarth, *Aust. Emerg. Nurs. J.*, 2017, **20**, 45–47.
20 M. Ali, A. Elsayed, A. Mendez, Y. Savaria and M. Sawan, *IEEE Sens. J.*, 2021, **21**, 14569–14586.
21 J. F. Fieselmann, M. S. Hendryx, C. M. Helms and D. S. Wakefield, *J. Gen. Intern. Med.*, 1993, **8**, 354–360.
22 G. Sierra, V. Telfort, B. Popov, L. G. Durand, R. Agarwal and V. Lanzo, *The 26th Annual International Conference of the IEEE Engineering in Medicine and Biology Society*, IEEE, San Francisco, CA, USA, 2004, vol. 3, pp. 317–320.
23 C. A. Kushida, M. R. Littner, M. Hirshkowitz, T. I. Morgenthaler, C. A. Alessi, D. Bailey, B. Boehlecke, T. M. Brown, J. Coleman, L. Friedman, S. Kapen, V. K. Kapur, M. Kramer, T. Lee-Chiong, J. Owens, J. P. Pancer, T. J. Swick and M. S. Wise, *Sleep*, 2006, **29**, 375–380.
24 L. K. Brown, *Clin. Chest Med.*, 1994, **15**, 715–727.
25 W. T. McNicholas, *J. Thorac. Dis.*, 2016, **8**, 236–242.
26 W. Y. Lim, C.-H. Goh, K. Z. Yap and N. Ramakrishnan, *Biosensors*, 2023, **13**, 209.
27 G. Song, T. Qin, H. Liu, G.-B. Xu, Y.-Y. Pan, F.-X. Xiong, K.-S. Gu, G.-P. Sun and Z.-D. Chen, *Lung Cancer*, 2010, **67**, 227–231.
28 M. Phillips, R. N. Cataneo, A. R. C. Cummin, A. J. Gagliardi, K. Gleeson, J. Greenberg, R. A. Maxfield and W. N. Rom, *Chest*, 2003, **123**, 2115–2123.
29 A. D. Subali, L. Wiyono, M. Yusuf and M. F. A. Zaky, *Diagn. Microbiol. Infect. Dis.*, 2022, **102**, 115589.

30 P. Zhu, Y. Liu, Z. Fang, Y. Kuang, Y. Zhang, C. Peng and G. Chen, *Langmuir*, 2019, **35**, 4834–4842.
31 C. L. Cao, C. G. Hu, L. Fang, S. X. Wang, Y. S. Tian and C. Y. Pan, *J. Nanomater.*, 2011, **2011**, 1–5.
32 M. S. Pawar, P. K. Bankar, M. A. More and D. J. Late, *RSC Adv.*, 2015, **5**, 88796–88804.
33 J. R. McGhee, J. S. Sagu, D. J. Southee and K. G. U. Wijayantha, *IEEE Sens. J.*, 2018, **18**, 7358–7364.
34 H.-E. Lin, Y. Katayanagi, T. Kishi, T. Yano and N. Matsushita, *RSC Adv.*, 2018, **8**, 30310–30319.
35 M. Deb, M.-Y. Chen, P.-Y. Chang, P.-H. Li, M.-J. Chan, Y.-C. Tian, P.-H. Yeh, O. Soppera and H.-W. Zan, *Biosensors*, 2023, **13**, 81.
36 B. Murali Babu and S. Vadivel, *J. Mater. Sci.: Mater. Electron.*, 2017, **28**, 2442–2447.
37 I. J. Tadeo, R. Parasuraman, S. B. Krupanidhi and A. M. Umarji, *Nano Express*, 2020, **1**, 010005.
38 S. Veeralingam, A. Gandrothula and S. Badhulika, *Mater. Res. Bull.*, 2023, **160**, 112133.
39 Y. H. Kim, S. J. Kim, Y.-J. Kim, Y.-S. Shim, S. Y. Kim, B. H. Hong and H. W. Jang, *ACS Nano*, 2015, **9**, 10453–10460.
40 Y. Liang, Q. Ding, H. Wang, Z. Wu, J. Li, Z. Li, K. Tao, X. Gui and J. Wu, *Nano-Micro Lett.*, 2022, **14**, 183.
41 K. Lazarova, S. Bozhilova, S. Ivanova, D. Christova and T. Babeva, *Sensors*, 2021, **21**, 3674.
42 J. Chu, X. Peng, P. Feng, Y. Sheng and J. Zhang, *Sens. Actuators, B*, 2013, **178**, 508–513.
43 A. S. Pawbake, R. G. Waykar, D. J. Late and S. R. Jadkar, *ACS Appl. Mater. Interfaces*, 2016, **8**, 3359–3365.
44 A. Beniwal, P. Ganguly, A. K. Aliyana, G. Khandelwal and R. Dahiya, *Sens. Actuators, B*, 2023, **374**, 132731.
45 S. Y. Park, J. E. Lee, Y. H. Kim, J. J. Kim, Y.-S. Shim, S. Y. Kim, M. H. Lee and H. W. Jang, *Sens. Actuators, B*, 2018, **258**, 775–782.
46 R. Zhou, J. Li, H. Jiang, H. Li, Y. Wang, D. Briand, M. Camara, G. Zhou and N. F. de Rooij, *Sens. Actuators, B*, 2019, **281**, 212–220.
47 P. M. Harrey, B. J. Ramsey, P. S. A. Evans and D. J. Harrison, *Sens. Actuators, B*, 2002, **87**, 226–232.
48 Y.-L. Tai and Z.-G. Yang, *Langmuir*, 2015, **31**, 13257–13264.
49 J.-M. Tulliani, B. Inserra and D. Ziegler, *Micromachines*, 2019, **10**, 232.
50 A. Kumar, G. Gupta, K. Bapna and D. D. Shivagan, *Mater. Res. Bull.*, 2023, **158**, 112053.
51 Y. Zheng, L. Sun, W. Liu, C. Wang, Z. Dai and F. Ma, *J. Mater. Chem. C*, 2020, **8**, 4206–4214.
52 C. Lv, C. Hu, J. Luo, S. Liu, Y. Qiao, Z. Zhang, J. Song, Y. Shi, J. Cai and A. Watanabe, *Nanomaterials*, 2019, **9**, 422.
53 A.-K. Herrmann, P. Formanek, L. Borchardt, M. Klose, L. Giebeler, J. Eckert, S. Kaskel, N. Gaponik and A. Eychmüller, *Chem. Mater.*, 2014, **26**, 1074–1083.
54 Y.-C. Chien, L.-Y. Huang, K.-C. Yang, M. R. Krishnan, W.-S. Hung, J.-C. Tsai and R.-M. Ho, *Emergent Mater.*, 2021, **4**, 493–501.
55 D. Navas, S. Fuentes, A. Castro-Alvarez and E. Chavez-Angel, *Gels*, 2021, **7**, 275.
56 F. Muench, *Catalysts*, 2018, **8**, 597.
57 S. S. Pathak and L. S. Panchakarla, *Appl. Mater. Today*, 2021, **24**, 101152.
58 C. N. R. Rao, G. U. Kulkarni, V. V. Agrawal, U. K. Gautam, M. Ghosh and U. Tumkurkar, *J. Colloid Interface Sci.*, 2005, **289**, 305–318.
59 G. Ramanath, J. D'Arcy-Gall, T. Maddanimath, A. V. Ellis, P. G. Ganesan, R. Goswami, A. Kumar and K. Vijayamohanan, *Langmuir*, 2004, **20**, 5583–5587.
60 M. D. Ho, Y. Liu, D. Dong, Y. Zhao and W. Cheng, *Nano Lett.*, 2018, **18**, 3593–3599.
61 K. Bramhaiah, V. N. Singh, C. Kavitha and N. S. John, *J. Nanosci. Nanotechnol.*, 2017, **17**, 2711–2719.
62 J.-P. Sylvestre, S. Poulin, A. V. Kabashin, E. Sacher, M. Meunier and J. H. T. Luong, *J. Phys. Chem. B*, 2004, **108**, 16864–16869.
63 D. Dias and J. Paulo Silva Cunha, *Sensors*, 2018, **18**, 2414.
64 B. Hill and S. H. Annesley, *Br. J. Nurs.*, 2020, **29**, 1.
65 B. Bhola, R. Kumar, I. Priyadarshini, C. So-In, T. Padhy, A. Slowik and A. H. Gandomi, *IEEE Sens. J.*, 2023, **23**, 18664–18674.
66 N. Ștefania Motoc, I. Făgărășan, A. E. Urda-Cîmpean and D. A. Todea, *Diagnostics*, 2023, **13**, 2597.
67 J. L. Ramírez, F. E. Annanouch, M. Camara, E. LLobet and D. Briand, *Procedia Eng.*, 2015, **120**, 707–710.